

Improved Stability-Based Transition Transport Model for Airships Incorporating Wall Heating Effects

Yayun Shi*

Xi'an Jiaotong University, Xi'an, Shaanxi, 710049, China

Qiyun Wang[†]

Northwestern Polytechnical University, Xi'an, Shaanxi, 710072, China

Xiaosong Lan[‡]

Xi'an Jiaotong University, Xi'an, Shaanxi, 710049, China

Bo Wang[§]

Qingdao Institute of Aeronautical Technology, Qingdao, Shandong, 266400, China

Tihao Yang[¶]

Northwestern Polytechnical University, Xi'an, Shaanxi, 710072, China

Yifu Chen^{||}

Delft University of Technology, Kluyverweg 1, 2629HS Delft, The Netherlands

Laminar drag reduction is a critical technology for enhancing the endurance and station-keeping capabilities of airship platforms. However, existing transport-based transition models fail to account for the premature transition induced by wall heating, a limitation that significantly hinders the robust engineering application of laminar-flow technology in realistic thermal environments. To address this deficiency, this study first develops stability-based correction for transition modeling that explicitly incorporates wall-to-freestream temperature ratios. Leveraging the Falkner–Skan–Cooke (FSC) equations and linear stability theory (LST) with the e^N method, we derive physics-based correlations for the transition criteria as functions of the temperature ratio, pressure gradient, and turbulence intensity. These corrections are integrated into a simplified stability-based transition transport model proposed by François et al. [1] and validated against the classic Schubauer and Klebanoff flat-plate experiments, demonstrating accurate prediction of transition locations under adiabatic, heated, and cooled conditions. Crucially, wind-tunnel experiments on a heated airship model show that wall-heating sensitivity is strongly influenced by local pressure-gradient variations, which is due to Reynolds-number-driven transition-location shifts. The proposed model successfully reproduces

*Associate Professor, State Key Laboratory for Strength and Vibration of Mechanical Structures, School of Aerospace Engineering.

[†]Master, National Key Laboratory of Aircraft Configuration Design, School of Aeronautics.

[‡]Master, State Key Laboratory for Strength and Vibration of Mechanical Structures, School of Aerospace Engineering.

[§]Research Fellow, Qingdao Institute of Aeronautical Technology.

[¶]Associate Research Fellow, National Key Laboratory of Aircraft Configuration Design, School of Aeronautics.

^{||}PhD candidate, Aerodynamics Group, Faculty of Aerospace Engineering. Email: y.chen-20@tudelft.nl (Corresponding Author)

the experimentally observed transition advancement caused by wall heating. This framework, covering both heating and cooling regimes, provides a capability to support future laminar-flow control technologies based on wall-temperature modulation.

Keywords: Transition transport modeling, Wall heating, Linear stability theory, Wall-to-freestream temperature difference effects, Laminar flow, Airship aerodynamics

I. Introduction

Stratospheric and high-altitude airships hold significant promise for both military and civil applications due to their exceptional endurance and station-keeping capabilities[2, 3]. Relative to conventional fixed-wing aircraft, these platforms offer superior energy efficiency and reduced operational costs[4, 5]. To maximize station-keeping capabilities, achieving superior aerodynamic efficiency is essential. Given their streamlined configuration (Fig. 1), implementing laminar-flow drag-reduction techniques becomes a primary strategy for realizing this performance goal. However, the operational environment introduces complex adverse factors; specifically, during daytime, solar usage and direct radiation can elevate the surface temperature significantly above ambient levels[6–8]. This wall heating fundamentally alters boundary-layer stability, causing premature laminar–turbulent transition (LTT) and severely compromising drag-reduction benefits. Consequently, accurate prediction of LTT location under realistic thermal conditions is a prerequisite for robust airship design.

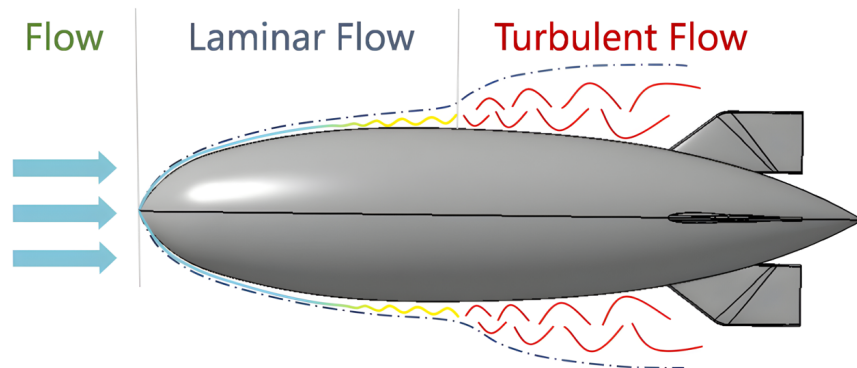


Fig. 1 The schematic diagram of laminar flow drag reduction on an airship.

The modulation of transition by wall temperature is highly dependent on the flow regime and the dominant instability mechanism[6, 7]. In hydrodynamic flows (water), wall heating typically stabilizes Tollmien-Schlichting (TS) waves, delaying transition[7, 9]. In high-speed aerodynamics, the effects are mode-dependent: for hypersonic flows, wall heating promotes first-mode instabilities but stabilizes second-mode disturbances[10–12], while in supersonic flows, heating generally triggers earlier transition[6]. Conversely, in the subsonic (low subsonic and transonic) regimes relevant to airships, wall heating has a distinct destabilizing effect, amplifying disturbances and advancing transition, whereas

wall cooling acts as a stabilizer[13, 14]. This study focuses specifically on quantifying and modeling this destabilizing behavior in the subsonic regime.

Across different flow regimes, the underlying transition mechanisms have mainly been investigated using direct numerical simulation (DNS) and stability-based approaches. Lv et al. [7] use the DNS to solve the laminar boundary layer equations with constant wall temperature conditions. With this base flow, the LST analysis is performed to study the effects of wall temperature on the disturbance growth and transition process. The simulation results agree very well with the experimental data. Fedorov et al. [15] employed DNS and LST approaches to investigate the hypersonic boundary-layer stability on a cone with localized wall heating/cooling, and the LST computation of the second-mode amplification agrees well with the DNS solutions. Similar approaches have also been applied in supersonic and subsonic flows [16, 17], and demonstrated that the stability analysis methods can accurately capture the heating/cooling effects.

However, stability-based transition prediction is computationally complex and difficult to apply directly to industrial three-dimensional configurations with complex geometries, such as the airship considered in this work. Meanwhile, the optimization of such configurations often requires numerous iterations, making stability-based methods impractical for routine use [18–21]. In contrast, correlation-based transport models such as the Langtry–Menter model[22], which rely solely on local flow variables and are well suited for parallel CFD and unstructured grids, have been widely adopted in industry. Similar transport-based transition models have also been extensively developed [23–25]. Consequently, a growing body of research aims to bridge this gap by deriving physics-informed corrections from high-fidelity datasets—generated via LST—and integrating them into transport models. This hybrid strategy allows for the accurate accounting of specific flow physics, such as crossflow or surface roughness, while retaining computational efficiency[26–32]. François et al. [1] recently proposed a simplified one-equation transition model based on the Langtry–Menter framework, which incorporates stability-based criteria for key transition parameters derived from LST analysis.

With regard to the effects of wall heating or cooling, related studies have already been carried out in hypersonic and underwater flows. In the hypersonic regime, Kovalev[33] incorporated the wall-temperature ratio as a correction factor into the Langtry–Menter transition criterion and investigated the influence of wall-to-freestream temperature difference on the transition location of hypersonic vehicles. For underwater vehicles, Shen et al. [34] combined the FSC equations with LST to calibrate key temperature-dependent transition parameters in the one equation model [1, 35] derived from the original two-equation Langtry–Menter formulation. The corrected model is able to accurately predict the transition location of underwater vehicles in the presence of boundary-layer temperature gradients.

For the airship configuration considered in this work, transport-based transition models are required to accelerate and simplify the aerodynamic shape optimization process. To the best of the authors' knowledge, no studies have yet incorporated the effects of wall heating into transport-based transition models for the subsonic airflows. As a result, when designing laminar airship configurations using such models, the influence of wall heating cannot be accounted for

in robust laminar-flow design. This, in turn, leads to overly optimistic estimates of laminar drag reduction, because the detrimental impact of wall heating is not accounted for the outset of the design process, preventing truly robust solutions from being obtained.

To address this deficiency, this work introduces a targeted correction to the simplified stability-based transport transition model proposed by François et al. [1], extending its validity to include generalized wall heating/cooling effects. Our methodology integrates novel transition criteria and local parameter correlations, derived via linear stability analysis (LST) and the e^N method, into this efficient transport-based framework. This physics-informed approach specifically captures the wall temperature modulation (both wall heating and wall cooling) of Tollmien-Schlichting (TS) waves—the primary instability mechanism governing transition on streamlined airship hulls at cruise angles of attack (0°). Further, we validate the improved model through a dedicated wind-tunnel experiment on a heated airship configuration. The experimental results provide direct confirmation that the proposed model accurately reproduces the significant upstream shift of the transition front induced by wall heating. As a result, this validated framework provides a robust engineering capability for the aerodynamic design and optimization of future laminar-flow platforms incorporating wall-temperature effects.

The remainder of this paper is structured as follows: Section II presents the theoretical formulation, encompassing the FSC equations, LST analysis, and the proposed corrections to the transition criteria. Section III details the implementation of the improved stability-based transport model and evaluates its performance against the conventional LST-based approach for typical cases. Section IV describes the wind-tunnel experiments and validates the improved transport model against experimental measurements from the heated airship configuration. Finally, Section V summarizes the key findings and conclusions.

II. Model Formulation

A. The Falkner-Skan-Cooke Boundary Layer Equations

Figure 2 illustrates an infinite swept wing along with two coordinate systems. The first is the wing-attached system, where the x -axis aligns with the wing chord and the z -axis extends along the spanwise direction. The second is the streamline coordinate system, in which x_s generally denotes the external potential flow direction. The angle between these two coordinate systems is denoted by ϕ . The three-dimensional compressible laminar boundary layer equations in

the wing-attached coordinate system are expressed as follows:

$$\begin{aligned}
 \text{Continuity: } & \frac{\partial}{\partial x}(\rho u) + \frac{\partial}{\partial y}(\rho v) = 0 \\
 x \text{ momentum: } & \rho \left(u \frac{\partial u}{\partial x} + v \frac{\partial u}{\partial y} \right) = \rho_e u_e \frac{\partial u_e}{\partial x} + \frac{\partial}{\partial y} \left(\mu \frac{\partial u}{\partial y} \right) \\
 z \text{ momentum: } & \rho \left(u \frac{\partial w}{\partial x} + v \frac{\partial w}{\partial y} \right) = \frac{\partial}{\partial y} \left(\mu \frac{\partial w}{\partial y} \right), \\
 \text{Energy: } & \rho c_p \left(u \frac{\partial T}{\partial x} + v \frac{\partial T}{\partial y} \right) + u \rho_e u_e \frac{du_e}{dx} = \frac{\partial}{\partial y} \left(\kappa \frac{\partial T}{\partial y} \right) + \mu \left(\frac{\partial u}{\partial y} \right)^2 + \mu \left(\frac{\partial w}{\partial y} \right)^2 \\
 \text{Gas state: } & p = \rho RT
 \end{aligned} \tag{1}$$

where u , v , and w denote the velocity components in the x , y , and z directions, respectively. T is the temperature, ρ is the density, μ is the dynamic viscosity, κ is the thermal conductivity, c_p is the specific heat at constant pressure, and R is the specific gas constant. The subscript e indicates the boundary-layer edge. The no-slip condition is enforced at the wall, combined with either an isothermal or adiabatic thermal condition. The corresponding boundary conditions are given by:

$$\begin{aligned}
 y = 0 : \quad & u = v = w = 0, \quad T = T_w \quad \text{or} \quad \frac{\partial T}{\partial y} = 0, \\
 y \rightarrow \infty : \quad & u \rightarrow u_e, v \rightarrow 0, w \rightarrow w_e, \quad T \rightarrow T_e.
 \end{aligned} \tag{2}$$

The subscript of w denotes the wall.

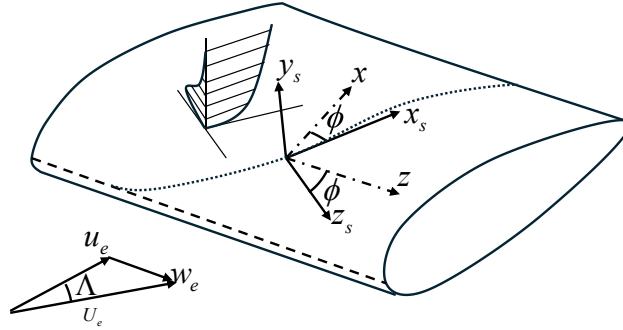


Fig. 2 Coordinate system used to formulate the compressible laminar boundary layer equations.

By introducing the similarity variables proposed by Falkner, Skan, and Cooke[36–38], the governing equations (Eq.(1)) can be rewritten as Eq.(3):

$$\begin{aligned}
 (\mathcal{N} f'')' + f f'' &= \frac{2m}{(m+1)} (f'^2 - \tau) \\
 (\mathcal{N} g')' + f g' &= 0 \\
 \frac{1}{Pr} (\mathcal{N} \tau')' + f \tau' &= 0 \\
 \mathcal{N} &= \tau^{1/2} \left(\frac{1 + T_s/T_e}{\tau + T_s/T_e} \right)
 \end{aligned} \tag{3}$$

known as the compressible Falkner-Skan-Cooke (FSC) equations, where

$$f(\eta) = \frac{u}{u_e}, \quad g(\eta) = \frac{w}{w_e}, \quad \tau(\eta) = \frac{T}{T_e} \quad \text{and} \quad \eta = y \sqrt{\frac{(m+1)u_e}{2\nu_e x}}. \quad (4)$$

The corresponding boundary conditions are:

$$\begin{aligned} \eta = 0 : f = f' = g = 0, \quad \tau = \tau_w \quad (\text{isothermal}) \quad \text{or} \quad \tau' = 0 \quad (\text{adiabatic}), \\ \eta \rightarrow \infty : f' = g = \tau = 1. \end{aligned} \quad (5)$$

Here, ν denotes the kinematic viscosity, Pr is the Prandtl number, and $\beta_h = 2m/(m+1)$ represents the Hartree pressure-gradient parameter. The resulting system of ordinary differential equations (ODEs) is solved locally using the Runge–Kutta method. For the numerical discretization, an equidistant grid is employed in the streamwise direction, while a Chebyshev spectral method is utilized in the wall-normal direction. Using the solution to the FSC equations, the velocity components projected along the external potential flow direction are expressed as:

$$\begin{aligned} u_s/Q_e &= f' \cos^2 \phi + g \sin^2 \phi \\ w_s/Q_e &= (g - f') \cos \phi \sin \phi \end{aligned} \quad (6)$$

In this study, we focus specifically on the streamwise velocity component, u_s . In Eq. (6), Q_e denotes the magnitude of the velocity vector at the boundary-layer edge.

B. The Linear Stability Theory Equations and e^N Method

The flow state variables are decomposed into the base flow quantities $\bar{\mathbf{q}} = (\rho, u, v, w, T)^T$ and perturbation quantities $\mathbf{q}' = (\rho', u', v', w', T')^T$. The base flow is assumed to be steady, spanwise invariant and local parallel, such that the perturbation growth is formulated by Linear Stability Theory (LST)[39], based on the ansatz expressed as

$$\mathbf{q}'(x, y, z, t) = \hat{\mathbf{q}}(y) \exp[i(\alpha x + \beta z - \omega t)] + \text{c.c.}, \quad (7)$$

where $\hat{\mathbf{q}}$ denote the 1-D perturbation shape functions in wall normal direction, α, β and ω are streamwise wavenumber, spanwise wavenumber and angular frequency, respectively. By inserting Eq. (7) into the linearized Navier–Stokes (LNS) equations, the governing partial differential equations are reduced into a coupled system of second-order ordinary differential equations, with dependence only on the wall-normal coordinates:

$$\mathcal{A}\hat{\mathbf{q}} + \mathcal{B}\frac{d\hat{\mathbf{q}}}{dy} + \mathcal{C}\frac{d^2\hat{\mathbf{q}}}{dy^2} = 0 \quad (8)$$

where $\mathcal{A}, \mathcal{B}, \mathcal{C}$ contains \bar{q}, α, β and ω . A spatial stability formulation is employed in which the spanwise wavenumber β and the angular frequency ω are specified a priori real number. The streamwise wavenumber α is unknown and complex, i.e. $\alpha = \alpha_r + i\alpha_i$, with its imaginary part quantifying the local rate of spatial amplification. Modal growth is therefore associated with negative values of α_i . Eq. (8) is a generalized complex eigenvalue problem with quadratic terms in α . Therefore, the companion matrix method[40] is needed to formulate a linear problem with respect to α , as expressed as

$$\mathbf{A}\tilde{\mathbf{q}} = \alpha\mathbf{B}\tilde{\mathbf{q}} \quad (9)$$

where $\tilde{\mathbf{q}} = (\hat{\mathbf{q}}, \alpha\hat{\mathbf{q}})^T$ and

$$\mathbf{A} = \begin{bmatrix} \mathcal{A} & -\mathcal{B} \\ 0 & \mathbf{I} \end{bmatrix}, \quad \mathbf{B} = \begin{bmatrix} 0 & \mathcal{C} \\ \mathbf{I} & 0 \end{bmatrix} \quad (10)$$

Once the local eigenvalue problems are all solved, the so-called N factor is obtained by integrating the local growth rate along the streamwise direction:

$$N = \int_x -\alpha_i dx \quad (11)$$

When having multiple frequencies and spanwise wavenumbers, the envelope of N factor is computed by

$$N_{\text{env}}(x, \beta) = \max_{\omega} (N(x, \omega, \beta)) \quad (12)$$

C. Transition Criteria With Wall-Temperature Effects

By combining the FSC equations, which account for boundary-layer temperature gradients, with linear stability theory, we calculate boundary-layer profiles and amplification factors across a range of temperature ratios (T_w/T_e) and pressure-gradient parameters (λ_θ). This extensive database enables the derivation of correlations between key transition-instability parameters (critical values) and their governing factors. For instance, while the original model correlated Re_{θ_t} solely with λ_θ and Tu , the present framework incorporates wall temperature effects. Without loss of generality, we consider both wall heating and cooling scenarios. To account for temperature ratio effects, we need establish a relation for Re_{θ_t} as a function of λ_θ , Tu , and T_w/T_e .

A critical component of the transition model is the local approximation of the momentum thickness Reynolds number Re_θ . In the original Langtry–Menter formulation, the ratio between the maximum vorticity Reynolds number ($\max(Re_{v,\max})$) and the momentum thickness Reynolds number (Re_θ) acts as a key parameter ($(Re_{v,\max})/Re_\theta = 2.193$) but neglects the influence of pressure gradients. To improve accuracy across a wider range of aerodynamic configurations, François et al. [1] refined this correlation by explicitly accounting for pressure-gradient effects ($(Re_{v,\max})/Re_\theta = f(\lambda_\theta)$).

Building on this approach, the present study further investigates and incorporates the influence of the wall-to-freestream temperature difference on this relationship ($(Re_{v,\max})/Re_\theta = f(\lambda_\theta, T_w/T_e)$).

In a summary, incorporating wall heating and cooling effects requires correcting two key model components: the ratio Π^+ between the maximum vorticity Reynolds number ($Re_{v,\max}$) and the momentum thickness Reynolds number (Re_θ), and the transition criterion $Re_{\theta t}$ for TS-wave-induced transition. The FSC analysis considers the wall-temperature ratio (T_w/T_e) and the pressure-gradient parameter (λ_θ) across a broad range of Reynolds numbers (up to 100×10^6). Coupled with linear stability theory, we compute the envelope curves of TS-wave amplification over a broad range of operating conditions: temperature ratios $T_w/T_e \in [0.7, 1.3]$, and parameters $m \in [-0.198, 1.0]$. The parameter m is related to the pressure-gradient parameter λ_θ employed in the transport model by the following equation:

$$\lambda_\theta = \frac{\theta^2 m u_e}{\nu_e x}. \quad (13)$$

The ratio $Re_{v,\max}/Re_\theta$ can be determined from boundary layer information. Fig. 3 (a) presents the contour plot of $(Re_{v,\max})/Re_\theta$ with respect to T_w/T_e and λ_θ , while Fig. 3 (b) shows the variation of $(Re_{v,\max})/Re_\theta$ with λ_θ at different T_w/T_e (T_r). In Fig. 3, the circular scatter points represent the data obtained based on the FSC equations, while the surface or solid lines are the fitted results. It can be observed that under heating conditions ($T_r > 1$), the ratio Π^+ increases with rising temperature ratio, whereas under cooling conditions, Π^+ decreases as the temperature ratio drops. We correct the ratio $\max(Re_{v,\max})/Re_\theta$ as follows:

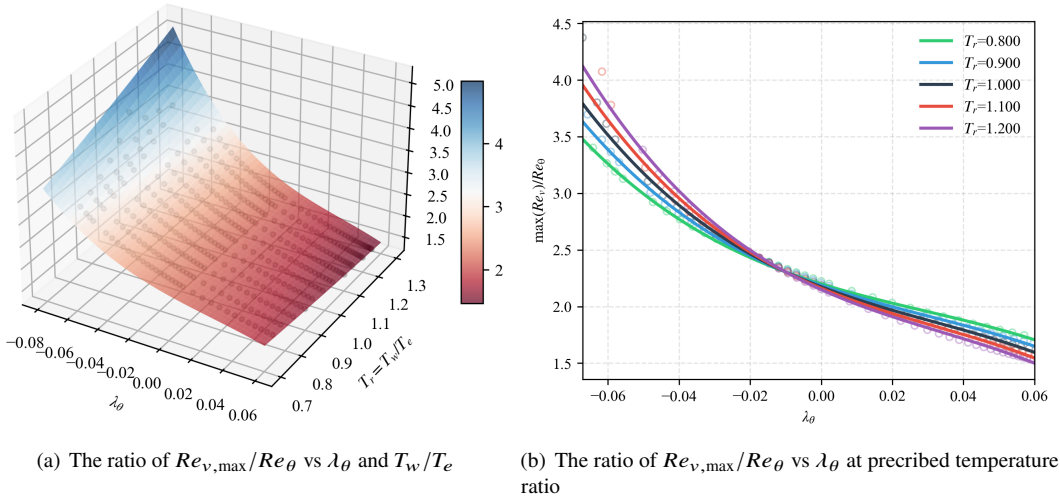


Fig. 3 The description of $Re_{v,\max}/Re_\theta$.

$$\begin{aligned}
\frac{Re_{v,\max}}{Re_\theta} = \Pi^+ = & \left(2.312813 + 0.8074101\lambda_\theta + 6.572101\lambda_\theta^2 - 352.2001\lambda_\theta^3 + 3.143236\lambda_\theta^4 \right) \\
& + T_r \left(-0.1514422 - 14.56479\lambda_\theta + 54.26127\lambda_\theta^2 - 368.1236\lambda_\theta^3 + 3.342443\lambda_\theta^4 \right) \\
& + T_r^2 \left(0.01279790 + 1.768478\lambda_\theta + 44.95197\lambda_\theta^2 - 391.6507\lambda_\theta^3 + 3.394677\lambda_\theta^4 \right).
\end{aligned} \tag{14}$$

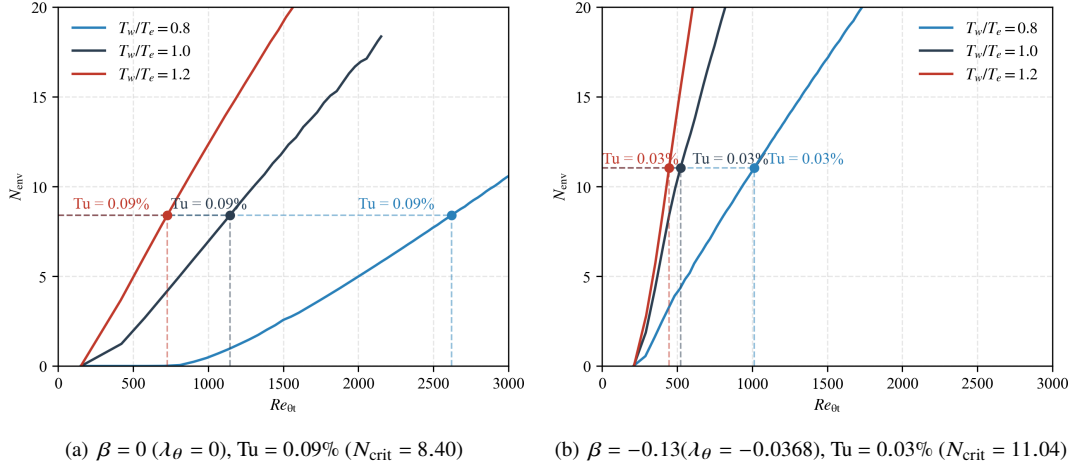


Fig. 4 The envelope curves of TS-wave amplification at fixed T_w/T_e and β over a range of momentum Reynolds number.

Based on different Tu , we can determine the critical momentum Reynolds number $Re_{\theta t}$ at transition location by using LST analysis and the e^N method (Fig. 4). The N_{crit} is determined by the turbulence intensity (Tu) by using Mack's relationship [39]

$$N_{crit} = -8.43 - 2.4 \ln(Tu). \tag{15}$$

In Fig. 4, the envelope curves of TS-wave amplification at fixed T_w/T_e and λ_θ over a range of momentum Reynolds number are presented. We can see that with the increase of wall temperature ratio (T_w/T_e), the transition location moves upstream, indicating that wall heating has a destabilizing effect on the boundary layer. The wall cooling has the opposite effect, and the critical $Re_{\theta t}$ increase significantly. Meanwhile, with the increase of adverse pressure gradient (more negative λ_θ), the transition location also moves upstream, indicating that the adverse pressure gradient has a destabilizing effect on the boundary layer.

We have 4024×600 (4024 corresponds to the combinations of temperature ratios, $Tu \in [0.0003, 0.003]$ and β (λ_θ) values, while the 600 refers solely to the distinct local Reynolds numbers) data points to fit the correction function of $Re_{\theta t}$ (the momentum thickness based Reynolds number at the transition location) with Tu , T_w/T_e and λ_θ . The results are shown in Fig. 5 and 6. Fig. 5 shows the variation of $Re_{\theta t}$ with λ_θ for prescribed T_r at different turbulence intensities, while Fig. 6 presents the surface of $Re_{\theta t}$ with λ_θ and T_r at different turbulence intensities. We show the results for two turbulence intensities ($Tu = 0.05\%$ and $Tu = 0.1\%$) as examples. The circular scatter points represent the data obtained

based on the FSC equations and LST stability analysis, while the curves and surfaces are the fitted results. The fitting accuracy is high, with \mathcal{R}^2 values exceeding 0.998 in all cases. We can see that the effect of cooling is significantly greater than that of heating. The influence of heating tends to saturate, regardless of whether the pressure gradient is adverse ($\lambda_\theta < 0$) or favorable ($\lambda_\theta > 0$). In general, $Re_{\theta t}$ increases as turbulence intensity decreases. It should be noted that the sensitivity of transition to wall temperature is considerably reduced under adverse pressure gradient conditions.

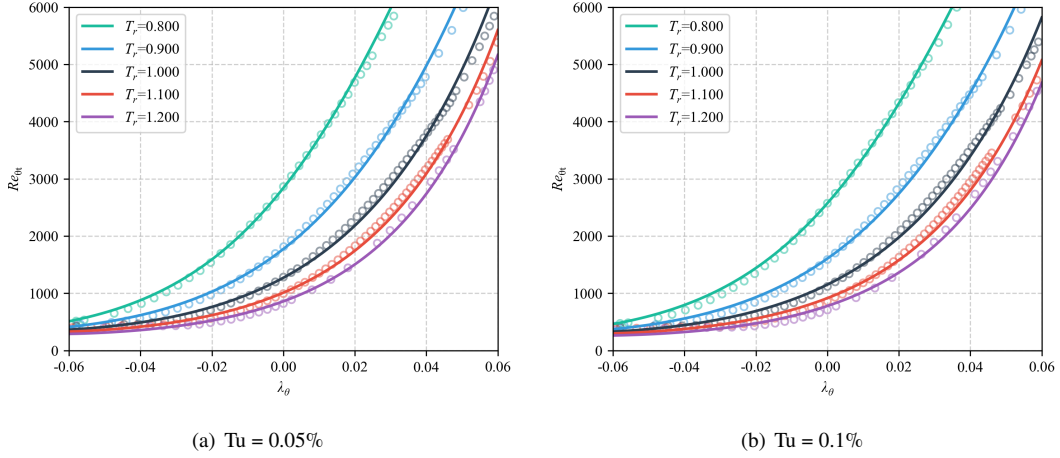


Fig. 5 Variation of $Re_{\theta t}$ with λ_θ for prescribed T_r at different turbulence intensities.

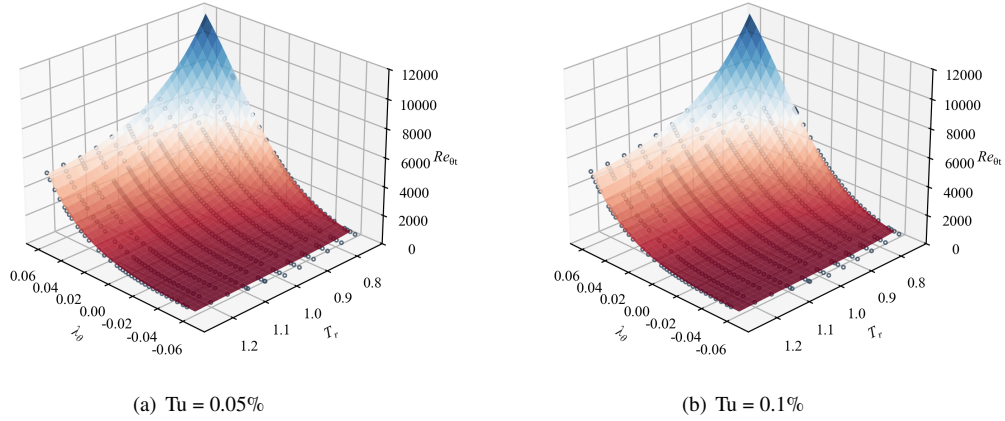


Fig. 6 The surface of $Re_{\theta t}$ with λ_θ and T_r at different turbulence intensities.

Finally, we obtain the correction function of $Re_{\theta t}$ as follows:

$$\ln(Re_{\theta t}) = \ln(h(\lambda_\theta, T_r)) + \ln(h(\text{Tu})), \quad (16)$$

where $\ln(h(\lambda_\theta, T_r))$ is expressed as:

$$\begin{aligned} \ln(h(\lambda_\theta, T_r)) = & \left(20.905432 - 34.936088 \lambda_\theta - 1162.249196 \lambda_\theta^2 - 792.760934 \lambda_\theta^3 + 5319.967633 \lambda_\theta^4 \right) \\ & + T_r \left(-30.666453 + 210.612461 \lambda_\theta + 1992.846133 \lambda_\theta^2 + 45.368047 \lambda_\theta^3 \right) \\ & + T_r^2 \left(22.766542 - 230.627111 \lambda_\theta - 798.668631 \lambda_\theta^2 \right) \\ & + T_r^3 \left(-5.872553 + 81.554132 \lambda_\theta \right), \end{aligned} \quad (17)$$

and $\ln(h(\text{Tu}))$ is defined as:

$$\ln(h(\text{Tu})) = 153.768618 + 82.899363 \ln(\text{Tu}) + 16.673825 [\ln(\text{Tu})]^2 + 1.485418 [\ln(\text{Tu})]^3 + 0.049537 [\ln(\text{Tu})]^4. \quad (18)$$

It can be observed that $h(\text{Tu})$ is a monotonically decreasing function.

III. Transport Transition Modeling and Validation

A. The Improved Stability-based Transition Transport Model

We used the stability-based transition modeling originally proposed by François et al. [1] as the base model. The transport equation of the intermittency γ in this modified model is expressed as:

$$\frac{\partial(\rho\gamma)}{\partial t} + \frac{\partial(\rho u_j \gamma)}{\partial x_j} = P_\gamma - E_\gamma + \frac{\partial}{\partial x_j} \left[\left(\mu + \frac{\mu_t}{\sigma_f} \right) \frac{\partial \gamma}{\partial x_j} \right], \quad (19)$$

where P_γ and E_γ are the production and destruction/relaminarization terms, respectively. σ_f is set to 1.0. The μ and μ_t are the laminar and turbulent dynamic viscosities, respectively. The production term is given as:

$$P_\gamma = F_{\text{length}} \rho S (1 - \gamma), \quad (20)$$

where F_{length} indicates the production rate of γ and is set as 14.0. S is the magnitude of the strain rate tensor. F_{onset} activates the production term when the local flow reaches the transition onset condition. In this study, we improve the definition of F_{onset} to consider wall-temperature effects, and it is defined as:

$$\begin{aligned} F_{\text{onset1}} &= \frac{\text{Re}_v}{\Pi^+ \text{Re}_{\theta t}}, \quad F_{\text{onset2}} = \min \left(\max \left(F_{\text{onset1}}, F_{\text{onset1}}^4 \right), 2.0 \right) \\ F_{\text{onset3}} &= \max \left(1 - \left(\frac{R_T}{2.0} \right)^3, 0.0 \right), \quad F_{\text{onset}} = \max \left(F_{\text{onset2}} - F_{\text{onset3}}, 0.0 \right), \\ R_T &= \frac{\mu_t}{\mu}, \quad \text{Re}_v = \frac{\rho d^2 S}{\mu} \end{aligned} \quad (21)$$

where F_{onset1} determines whether the local flow has reached the transition onset condition. Here, $Re_{\theta t}$ is calculated using Eqs. (16), (17), and (18) in Section II. It depends on the freestream turbulence intensity (Tu), the pressure gradient parameter (λ_θ), and the wall-to-freestream temperature ratio (T_w/T_e). The term Re_v/Π^+ represents the local momentum thickness Reynolds number Re_θ , as defined in Eq. (14). In Eq. (21), Re_v is the vorticity Reynolds number, d is the distance to the nearest wall, and the wall-to-freestream temperature ratio (T_w/T_e) is considered.

The pressure gradient parameter λ_θ is defined as:

$$\lambda_\theta = \frac{\rho\theta^2}{\mu} \frac{dQ_e}{ds} = Re_\theta^2 \frac{v_e}{Q_e^2} \frac{dQ_e}{ds}, \quad (22)$$

where Re_θ is computed by $(Re_v)/\Pi^+$ (14). In Eq. (22), dQ_e/ds is given by

$$\frac{dQ_e}{ds} = \frac{u}{Q_e} \frac{dQ_e}{dx} + \frac{v}{Q_e} \frac{dQ_e}{dy} + \frac{w}{Q_e} \frac{dQ_e}{dz}, \quad (23)$$

where Q_e is the magnitude of the velocity vector at the boundary-layer edge and computed from the compressible Bernoulli equation and is expressed as:

$$Q_e = \sqrt{U_\infty^2 + \frac{2\kappa_r}{\kappa_r - 1} \left[1 - \left(\frac{p}{p_\infty} \right)^{(\kappa_r - 1)/\kappa_r} \right] \frac{p_\infty}{\rho_\infty}}, \quad (24)$$

where κ_r is the ratio of specific heats. The edge-velocity gradients in the three coordinate directions are calculated using the external potential flow pressure gradients as follows:

$$\begin{aligned} \frac{dQ_e}{dx} &= -\frac{1}{\rho_\infty Q_e} \frac{p}{p_\infty}^{-1/\kappa_r} \frac{dp}{dx}, \\ \frac{dQ_e}{dy} &= -\frac{1}{\rho_\infty Q_e} \frac{p}{p_\infty}^{-1/\kappa_r} \frac{dp}{dy}, \\ \frac{dQ_e}{dz} &= -\frac{1}{\rho_\infty Q_e} \frac{p}{p_\infty}^{-1/\kappa_r} \frac{dp}{dz}. \end{aligned} \quad (25)$$

As the formulation of the edge-velocity gradient in the streamwise direction is not Galilean-invariant, it can be only applied to fixed-wall configurations.

We improve Π^+ as Eq. (14) to consider the temperature difference. We can see the temperature difference has a significant effect on Π^+ (Fig. 3), which further influences the transition onset function F_{onset} . The T_w and T_e are calculated by the local temperature and freestream temperature (the unit is K). In Eq. (21), F_{onset2} ensures a rapid growth of intermittency once the transition onset condition is met, while F_{onset3} accounts for the damping effect of

existing turbulence in the boundary layer. The destruction/relaminarization term E_γ is expressed as:

$$E_\gamma = c_{a2}\rho\Omega\gamma F_{\text{turb}} (c_{e2}\gamma - 1), \quad (26)$$

where C_{a2} and C_{e2} are model constants set to 1.0 and 50.0, respectively. The Ω is the magnitude of vorticity, and F_{turb} is a function that activates the destruction term in turbulent regions, given by

$$F_{\text{turb}} = \exp \left[- \left(\frac{R_T}{4} \right)^4 \right]. \quad (27)$$

The intermittency γ is then used to modify the production term of the $k - \omega$ shear-stress transport (SST) turbulence model [41, 42], effectively activating the turbulence production in the transition and turbulent regions. It consists in modifying the production term of the turbulent kinetic energy (k) equation as follows:

$$\frac{\partial}{\partial t}(\rho k) + \frac{\partial}{\partial x_j}(\rho u_j k) = \tilde{P}_k - \tilde{D}_k + \frac{\partial}{\partial x_j} \left[(\mu + \sigma_k \mu_t) \frac{\partial k}{\partial x_j} \right], \quad (28)$$

where $\tilde{P}_k = \gamma P_k$ and $\tilde{D}_k = \min[\max(\gamma, 0.1), 1.0] D_k$. The production of k is suppressed in laminar and transitional regions by the intermittency γ , while the destruction term is only partially suppressed in laminar regions to avoid numerical issues. When γ is 1.0, the original $k - \omega$ SST model is recovered.

B. Comparison of the Improved Model with LST-based Approach for Typical Cases

We chose the Schubauer and Klebanoff (SK) flat plate to compare the results of the improved model with those from LST [43]. The SK flat plate is a classic experiment of transition induced by TS instabilities. The velocity is 50m/s , the turbulence intensity is 0.1%, and unit Reynolds number is 3.34×10^6 . The computational grid used in this study and the boundary conditions are shown and set as Fig. 7. The grid mesh consists of 361 points in the streamwise direction and 161 points in the normal direction, with y^+ values of 0.2 and growth ratio of 1.12.

We present the comparison results between present improved model, LST results (starting points), and experimental result at the adiabatic wall temperature in Fig. 8. The skin friction coefficient (C_f) is used to determine the transition location, which is indicated by a sharp rise in C_f . The horizontal axis represents the local Reynolds number. The solid lines present improved model, the circle indicates the starting transition point of the LST-based results, and the squares indicate the experimental results. For the LST results, the transition location is determined by the e^N method with $N_{\text{crit}} = 8.14$. It can be seen that the improved model and LST result accurately capture the transition location compared to the experimental results, and the prediction error ($\Delta x_{\text{tr}}/c$) is lower than 5%. The results with adiabatic conditions and wall heating ($T_w/T_e = 1.05$ and $T_w/T_e = 1.15$) are shown in Fig. 9. The improved model matches well LST results at wall heating conditions. The transition location moves upstream as the wall temperature increases, indicating that

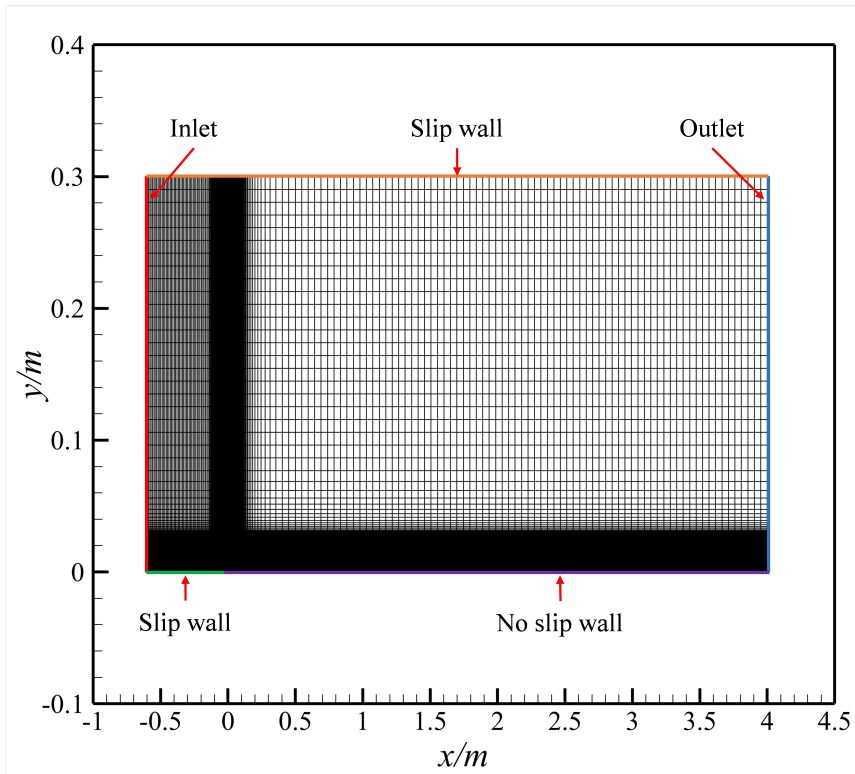


Fig. 7 The flat plate computational grid for the SK case.

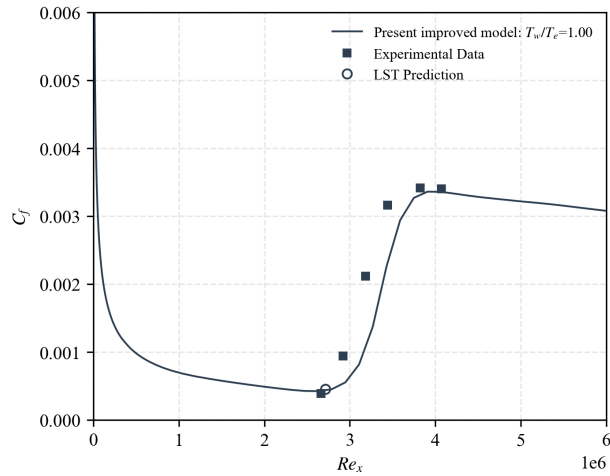


Fig. 8 Comparison of skin friction among the improved model, LST, and experimental results at the adiabatic wall temperature.

wall heating has a significant destabilizing effect on the boundary layer. Specifically, at $T_w/T_e = 1.15$, the laminar flow region is reduced by approximately half. The results for the wall-cooling cases ($T_w/T_e = 0.85$ and $T_w/T_e = 0.75$) are presented in Fig. 10. The improved model also demonstrates excellent agreement with LST predictions under these cooling conditions. For $T_w/T_e = 0.85$, the transition location shifts significantly downstream, confirming the

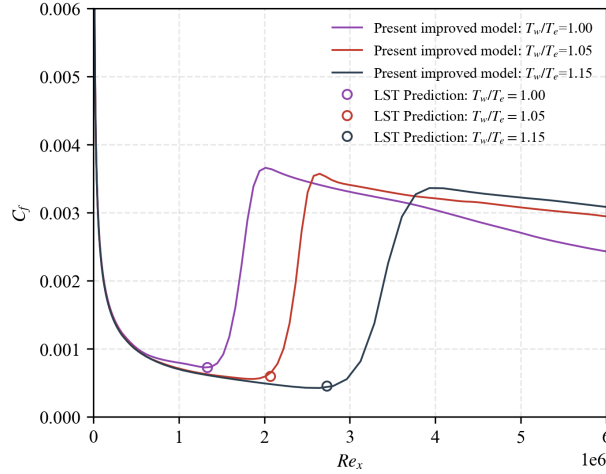


Fig. 9 Comparison of skin friction among the improved model and LST results at the cooled wall temperature.

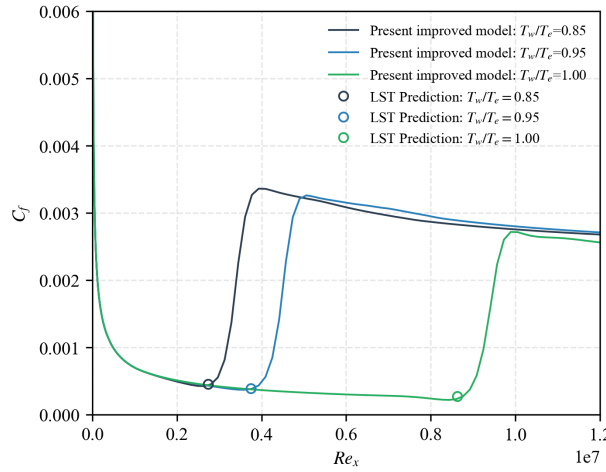


Fig. 10 Comparison of skin friction among the improved model and LST results at the heated wall temperature.

strong stabilizing effect of wall cooling on the boundary layer. In summary, the improved model accurately captures the sensitivity of the transition location to wall temperature variations. Compared with LST results, the transition location prediction errors ($\Delta x_{tr}/c$) of the improved model are within 5% for all cases.

To further illustrate the effects of wall heating and cooling on boundary layer characteristics, we present the boundary layer velocity and temperature profiles at different wall-to-ambient temperature ratios in Fig. 11. The velocity profiles are non-dimensionalized by the edge velocity u_e , while the temperature profiles are non-dimensionalized by the edge temperature T_e . From Fig. 11(a), we observe that wall heating leads to a fuller velocity profile with a higher shape factor, indicating a more unstable boundary layer. Conversely, wall cooling results in a more pronounced velocity gradient near the wall, signifying a more stable boundary layer. Fig. 11(b) shows that wall heating increases the temperature throughout the boundary layer, while wall cooling decreases it. These changes in temperature profiles further influence

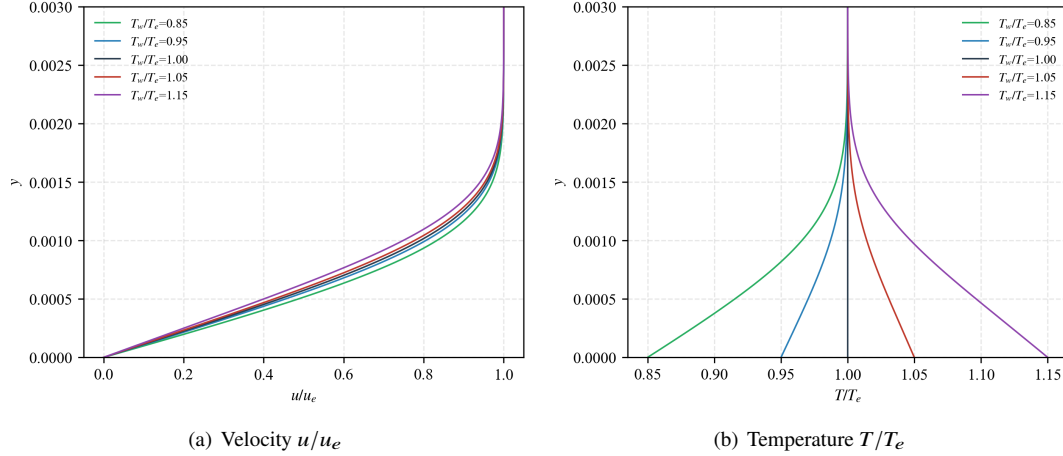


Fig. 11 The boundary layer velocity and temperature (non-dimensional) comparisons at different temperature difference ratios.

the viscosity and density distributions, thereby affecting the stability characteristics of the boundary layer. Overall, the boundary layer profiles corroborate the observed trends in transition locations, highlighting the destabilizing effect of wall heating and the stabilizing effect of wall cooling.

IV. The Wind Tunnel Test and validation of Improved Model for the Heated Airship

We conducted experiments on the designed airship in the FL-52 wind tunnel. Considering that the real airship's surface primarily experiences heating, the focus of the experiments is to measure the LLT changes after heating. Furthermore, we validated our improved model to test whether it can capture the impact of heating on transition in a real three-dimensional configuration.

A. The Wind Tunnel Test of the Heated Airship

The wind tunnel experiments are conducted using the FL-52 wind tunnel open test section platform with a semi-curved blade angle mechanism to support the model, as shown in the Fig. 12. An infrared thermography camera was used to measure the surface temperature, and the transition location was determined based on the temperature gradient. The tests were conducted at ambient temperature (T_e 288.15K) and heating conditions. In the heating tests, the model was first heated to 343.34K and then to 371.29K at 50m/s, and to 345.92K and 366.35 at 75m/s using heating films inside the model. The wind tunnel experiments were then conducted, as shown in Fig. 13. The reference length of the model is 1.4m, and the reference chord length is $0.2m^2$. The test angle of attack are 0° , and the test speeds include 50m/s and 75m/s. The turbulence intensity of the wind tunnel is 0.08%.

Figures 14 and 15 present the infrared thermography results across various test conditions. The experimental methodology relies on the principle that turbulent boundary layers sustain significantly higher convective heat transfer



(a) The wind tunnel test setup

(b) The airship model

Fig. 12 The wind tunnel test setup for the airship.

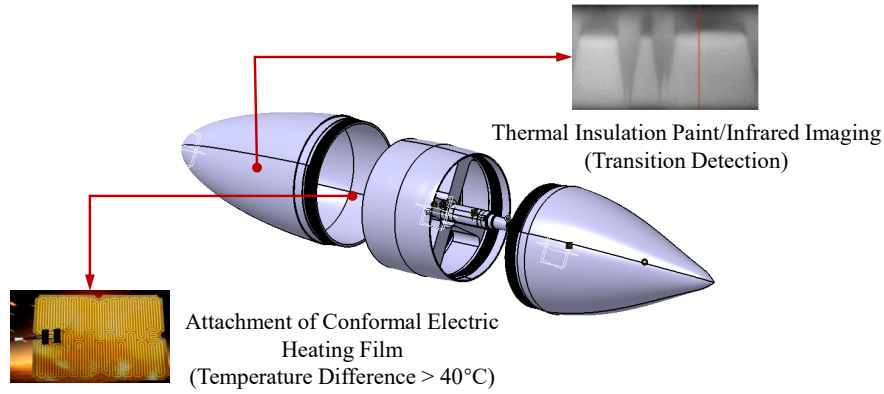
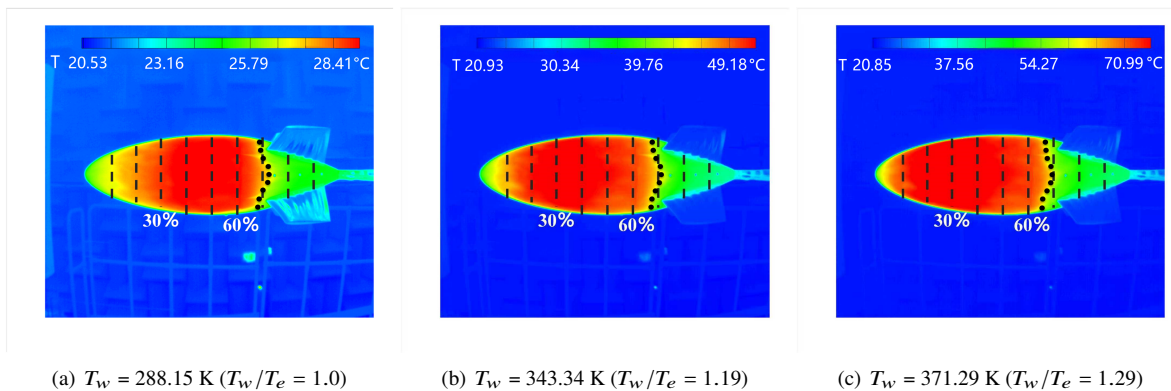


Fig. 13 The schematic diagram of heating film and transition detection on the airship model.

rates than their laminar counterparts. Following wall heating, the surface is allowed to cool, during which the laminar–turbulent transition front is detected by identifying the abrupt variation in the streamwise surface temperature gradient. These transition onset points correspond to the distinct steepening of the temperature decay and are explicitly marked with black dots in Figs. 14 and 15.



(a) $T_w = 288.15 \text{ K}$ ($T_w/T_e = 1.0$)

(b) $T_w = 343.34 \text{ K}$ ($T_w/T_e = 1.19$)

(c) $T_w = 371.29 \text{ K}$ ($T_w/T_e = 1.29$)

Fig. 14 The infrared temperature results at $V = 50 \text{ m/s}$.

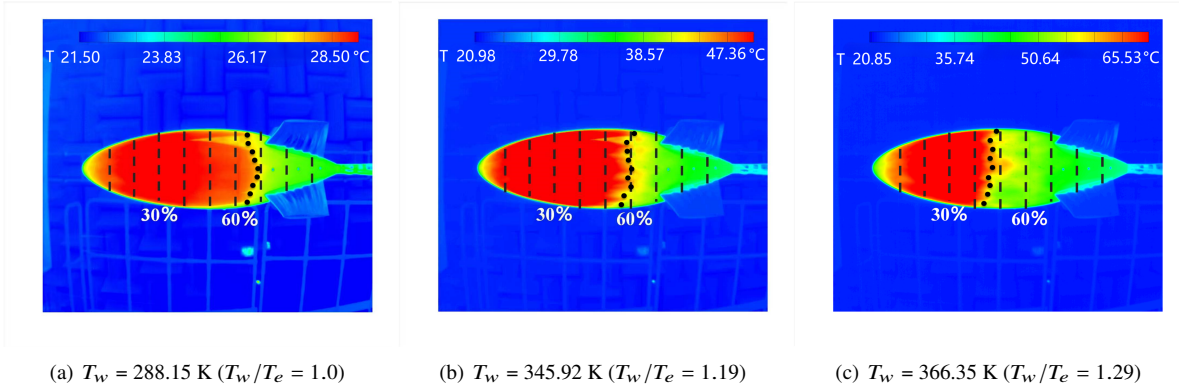


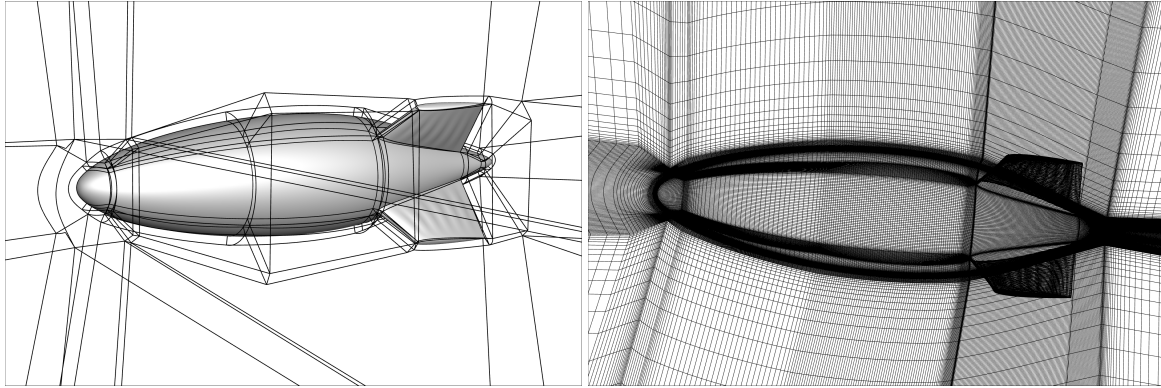
Fig. 15 The infrared temperature results at $V = 75 \text{ m/s}$.

From the infrared temperature results, it can be observed that as the surface temperature of the airship increases, the transition location moves forward. The results indicate that heating promotes the transition process on the airship surface. At a velocity of 50 m/s (corresponding to a unit Reynolds number of 3.359×10^6), the impact of heating on the transition location is marginal. However, as the velocity increases to 75 m/s (corresponding to a unit Reynolds number of 5.039×10^6), heating exerts a significantly more pronounced effect on the transition location, as shown in Figure 15. This sensitivity is governed by the Reynolds number and the pressure gradient near the transition front. A detailed analysis of the pressure gradient contribution is presented in Section IV.B. At 75 m/s , a wall-temperature increase of 57.77 K shifts the transition location upstream by approximately 10%. When the temperature increase reaches 78.2 K , the transition location advances by about 25%.

B. Validation of the Improved Stability-based Model

Based on the experimental results, we validate our improved model. The model and computational mesh are shown in the Fig. 16. The grid size (half model) is 9,619,200 cells. The first layer in the wall-normal direction has $y^+ = 0.8$, with a growth rate of 1.15. The simulation results using the present improved model are shown in Fig. 17 and 18. In Fig. 17 and 18, the solid lines represent the simulation average transition locations at the streamwise direction, while the black solid circles indicate the experimental results. It can be observed that under different velocities and heating conditions, the computational results agree well with the experimental data. Compared with the experiments, the relative error is between 2% and 6%. We also simulate the intermittency model proposed by François et al. [1], the simulation results and experimental comparisons are shown in Fig. 19. The transition locations at different wall temperatures are almost identical, which contradicts the experimental results. This demonstrates the necessity of accounting for the effect of temperature differences, thereby capturing its impact on the transition location and laminar region.

Here, we elucidate a critical phenomenon mentioned in Section IV.A: at a velocity of 50 m/s , the transition location remains virtually unchanged with wall heating. However, at 75 m/s , the transition location shifts significantly under



(a) The model and mesh topology

(b) The surface mesh

Fig. 16 The computation mesh for the airship.

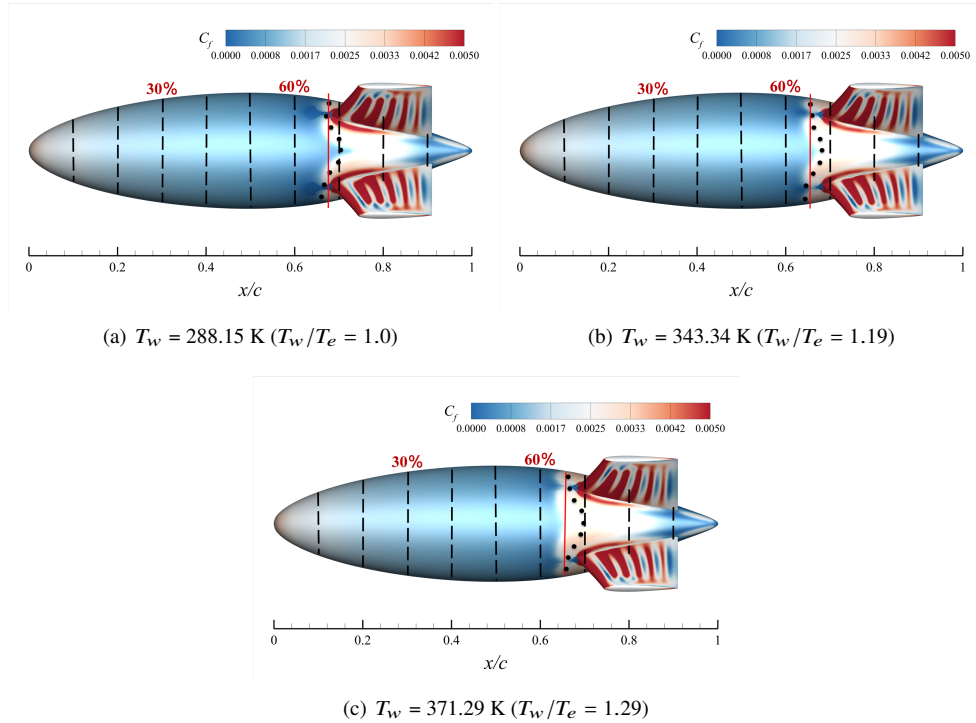


Fig. 17 The transition locations comparison between present improved model and experimental results at $V = 50 \text{ m/s}$.

heating conditions. Fig. 20 illustrates the pressure distributions corresponding to different velocities. At 50 m/s , transition occurs in the adverse pressure gradient (APG) region, whereas at 75 m/s , due to the increased Reynolds number, transition occurs in the zero or weak favorable pressure gradient (FPG) region. As shown in Fig. 5, in the APG region, wall heating has a minimal impact on the transition momentum thickness Reynolds number (Re_{θ_t}). Furthermore, the boundary layer in the APG region is thicker, requiring only a short streamwise distance to reach the critical Re_{θ_t} . In contrast, in the weak FPG or near-zero pressure gradient region, wall heating significantly impacts Re_{θ_t} . The

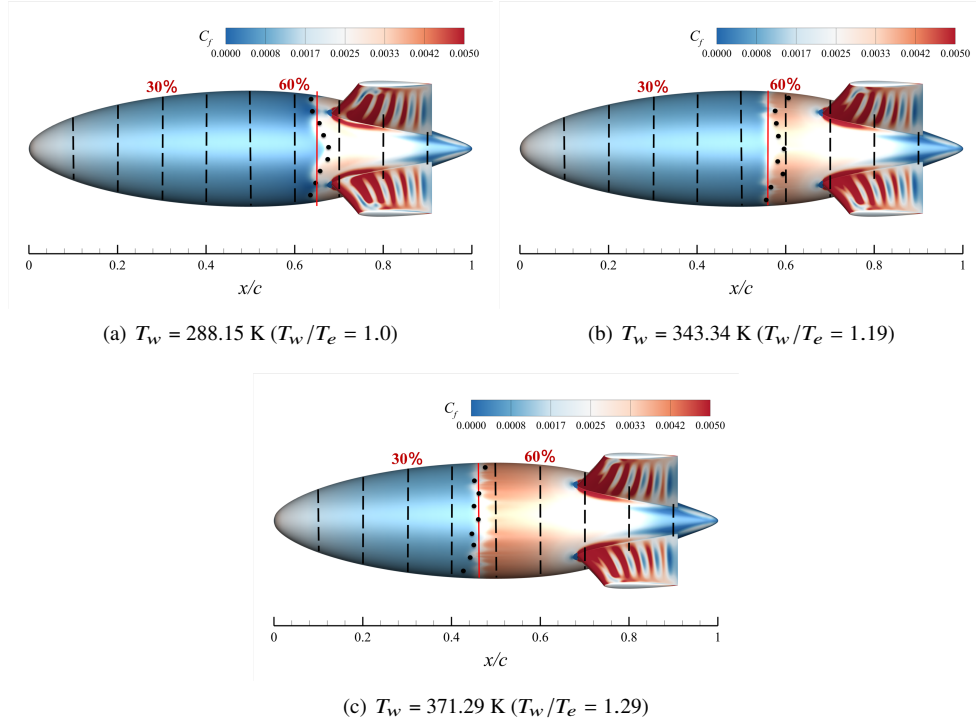


Fig. 18 The transition locations comparison between present improved model and experimental results at $V = 75 \text{ m/s}$.

corresponding boundary layer is thinner, necessitating a longer streamwise distance to attain the critical $Re_{\theta t}$. Thus, the combined effects of Reynolds number and local pressure gradient determine the influence of wall heating on the airship transition location. Since the Reynolds numbers encountered in real airship flight are typically high, airships are therefore prone to surface-heating effects during daytime operation, which can degrade the drag-reduction performance. Consequently, the wall-heating effect must be considered. With this improved transition model, we can proactively consider the adverse effects of daytime heating in future airship designs and develop aerodynamic shapes that can resist the shortening of the laminar region during the day, thus achieving robust laminar flow design.

V. Conclusions

Laminar drag reduction is an important means of reducing airship drag. However, during daytime operation, solar panels on the airship surface can raise the wall temperature far above the ambient temperature, leading to a wall-heating effect. Existing transport-based transition models have not yet accounted for this phenomenon. To address this issue, the main contributions of this work are as follows:

- 1) We conducted a series of linear stability theory (LST) analyses on FSC boundary layers under various wall-to-freestream temperature ratios, freestream turbulence intensities, and pressure gradient conditions. Based on the LST results, we developed a correction for the critical Reynolds number based on momentum thickness

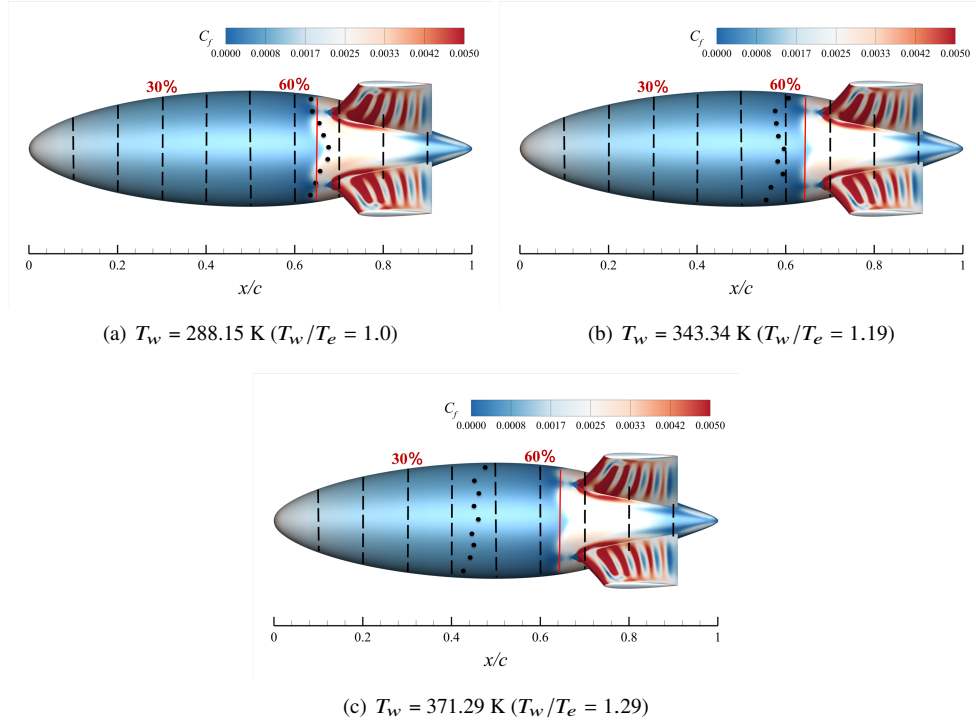


Fig. 19 The transition locations comparison by using the one-equation model proposed by François et al. [1] and experimental results at $V = 75m/s$.

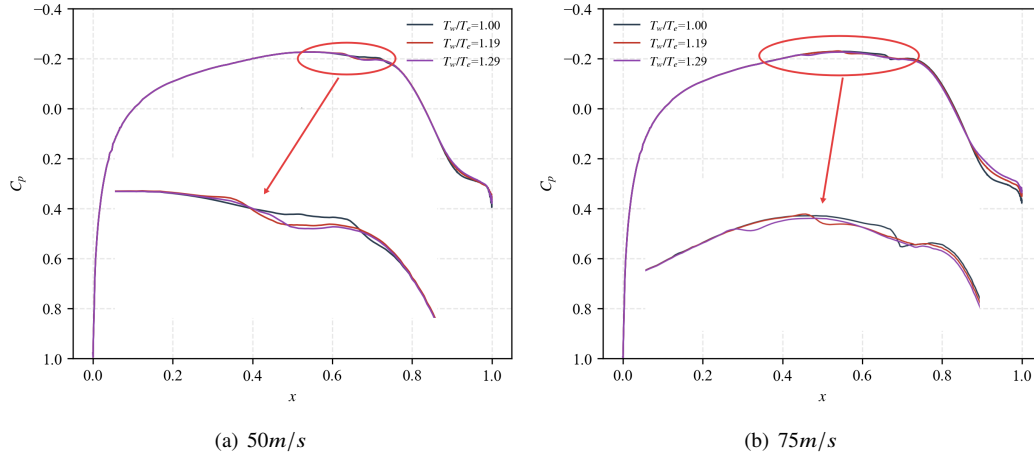


Fig. 20 The pressure coefficient distribution along the streamwise direction for the airship.

$(Re_{\theta t})$ and the key parameter of $Re_{v,max}/Re_{\theta}$ to account for wall-heating effects. Besides, we also consider the wall-cooling effects. The correction shows that wall heating reduces $Re_{\theta t}$, promoting earlier transition, while wall cooling increases $Re_{\theta t}$, delaying transition.

- 2) We integrated the improved $Re_{\theta t}$, $Re_{v,max}/Re_{\theta}$ into the intermittency transport modeling [1]. For the Schubauer and Klebanoff flat-plate case, we compared the improved model predictions with LST results under adiabatic,

wall-cooling, and wall-heating conditions. The results demonstrate excellent agreement, with relative errors within 5%. Besides, the improved model and LST prediction agree well with the experimental result at the adiabatic condition. This indicates that the improved model can accurately capture the effects of the wall-to-ambient temperature difference on transition.

- 3) Most importantly, we performed wind tunnel experiments on a heated airship model to investigate the effect of wall heating on transition location. The experimental results demonstrate that the impact of wall heating is governed by the combined effects of the Reynolds number and the local pressure gradient. Specifically, in the adverse pressure gradient region, the transition location is insensitive to wall heating; however, as the Reynolds number increases and the transition front moves into the favorable or zero pressure gradient region, wall heating significantly shifts the transition location upstream. We then validated the improved transition model against the experimental data, showing good agreement (relative errors no more 6%) and confirming its effectiveness in capturing the influence of wall heating on transition.

Our improved stability-based transition model accounts for the effects of wall heating and wall cooling, providing an important transition-prediction approach to support future laminar-flow control for flight vehicles. In future work, we will extend the study to include crossflow instability and its dependence on wall cooling/heating temperature.

Acknowledgments

This work was supported by the National Natural Science Foundation of China under grant number 12302302, 52572421 and the Taishan Scholars Program.

The authors acknowledge the assistance of AI for language polishing and improving the clarity of the manuscript.

References

- [1] François, D. G., Krumbein, A., Krimmelbein, N., and Grabe, C., “Simplified stability-based transition transport modeling for unstructured computational fluid dynamics,” Journal of Aircraft, Vol. 60, No. 6, 2023, pp. 1773–1784.
- [2] Ilieva, G., Páscoa, J. C., Dumas, A., and Trancossi, M., “A critical review of propulsion concepts for modern airships,” Central European Journal of Engineering, Vol. 2, No. 2, 2012, pp. 189–200.
- [3] Liao, L., and Pasternak, I., “A review of airship structural research and development,” Progress in Aerospace Sciences, Vol. 45, No. 4-5, 2009, pp. 83–96.
- [4] Zuo, Z., Song, J., Zheng, Z., and Han, Q.-L., “A survey on modelling, control and challenges of stratospheric airships,” Control Engineering Practice, Vol. 119, 2022, p. 104979.
- [5] Wu, J., Fang, X., Wang, Z., Hou, Z., Ma, Z., Zhang, H., Dai, Q., and Xu, Y., “Thermal modeling of stratospheric airships,” Progress in Aerospace Sciences, Vol. 75, 2015, pp. 26–37.

- [6] Celep, M., Hadjadj, A., Shadloo, M. S., Sharma, S., Yildiz, M., and Kloker, M., “Effect of streak employing control of oblique-breakdown in a supersonic boundary layer with weak wall heating/cooling,” Physical Review Fluids, Vol. 7, No. 5, 2022, p. 053904.
- [7] Lv, J., Zhang, Y., and Liu, J., “Numerical investigation on the natural transition of boundary layers on an underwater axisymmetric body with heated/cooled walls,” Physics of Fluids, Vol. 37, No. 2, 2025.
- [8] Kral, L., and Fasel, H., “Direct numerical simulation of passive control of three-dimensional phenomena in boundary-layer transition using wall heating,” Journal of Fluid Mechanics, Vol. 264, 1994, pp. 213–254.
- [9] Lv, J., and Zhang, Y., “Numerical study of the natural transition of water boundary layers over heated/cooled flat plates,” Physics of Fluids, Vol. 35, No. 6, 2023.
- [10] Zhao, R., Wen, C., Tian, X., Long, T., and Yuan, W., “Numerical simulation of local wall heating and cooling effect on the stability of a hypersonic boundary layer,” International Journal of Heat and Mass Transfer, Vol. 121, 2018, pp. 986–998.
- [11] Liu, Z., Lu, Y., Liang, J., and Huang, H., “Roughness-Induced Transition in Supersonic Boundary Layers with Wall Heating and Cooling Effects,” AIAA Journal, Vol. 62, No. 7, 2024, pp. 2458–2475.
- [12] Xu, J., and Liu, J., “Wall-cooling effects on secondary instabilities of Mack mode disturbances at Mach 6,” Physics of Fluids, Vol. 34, No. 4, 2022.
- [13] Manuilovich, S., and Ustinov, M., “Heat addition effect on the instability of the crossflow in a three-dimensional boundary layer,” Fluid Dynamics, Vol. 49, No. 5, 2014, pp. 602–607.
- [14] Lopez, M. B., van de Weijer, A., Vidales, A. R., and Kotsonis, M., “Impact of a Heated Wall on the Laminar-to-Turbulent Transition of Crossflow Vortices: an Experimental Study,” AIAA SCITECH 2024 Forum, American Institute of Aeronautics and Astronautics Inc.(AIAA), 2024, pp. AIAA–2024.
- [15] Fedorov, A., Soudakov, V., Egorov, I., Sidorenko, A., Gromyko, Y., Bountin, D., Polivanov, P., and Maslov, A., “High-speed boundary-layer stability on a cone with localized wall heating or cooling,” AIAA Journal, Vol. 53, No. 9, 2015, pp. 2512–2524.
- [16] Poulain, A., Content, C., Rigas, G., Garnier, E., and Sipp, D., “Adjoint-based linear sensitivity of a supersonic boundary layer to steady wall blowing–suction/heating–cooling,” Journal of Fluid Mechanics, Vol. 978, 2024, p. A16.
- [17] Thummar, M., Bhoraniya, R., and Narayanan, V., “Stability and receptivity analyses of the heated flat-plate boundary layer with variable viscosity,” International Journal of Heat and Fluid Flow, Vol. 110, 2024, p. 109624.
- [18] Shi, Y., Mader, C. A., He, S., Halila, G. L. O., and Martins, J. R. R. A., “Natural Laminar-Flow Airfoil Optimization Design Using a Discrete Adjoint Approach,” AIAA Journal, Vol. 58, No. 11, 2020, pp. 4702–4722. <https://doi.org/10.2514/1.J058944>.
- [19] Shi, Y., Mader, C. A., and Martins, J. R. R. A., “Natural Laminar Flow Wing Optimization Using a Discrete Adjoint Approach,” Structural and Multidisciplinary Optimization, Vol. 64, No. 2, 2021, pp. 541–562.

- [20] Shi, Y., Song, C., Chen, Y., Rao, H., and Yang, T., “Complex standard eigenvalue problem derivative computation for laminar–turbulent transition prediction,” AIAA Journal, Vol. 61, No. 8, 2023, pp. 3404–3418.
- [21] Yifu, C., Hanyue, R., Neng, X., Jun, F., Yayun, S., and Tihao, Y., “Adjoint-based robust optimization design of laminar flow airfoil under flight condition uncertainties,” Aerospace Science and Technology, 2023, p. 108465.
- [22] Langtry, R. B., and Menter, F. R., “Correlation-Based Transition Modeling for Unstructured Parallelized Computational Fluid Dynamics Codes,” AIAA Journal, Vol. 47, No. 12, 2009, pp. 2894–2906. <https://doi.org/10.2514/1.42362>.
- [23] Coder, J. G., and Maughmer, M. D., “Computational Fluid Dynamics Compatible Transition Modeling Using an Amplification Factor Transport Equation,” AIAA Journal, Vol. 52, No. 11, 2014, pp. 2506–2512. <https://doi.org/10.2514/1.J052905>.
- [24] Krimmelbein, N., and Krumbein, A., “Validation of transition modeling techniques for a simplified fuselage configuration,” Aerospace Science and Technology, Vol. 118, 2021, p. 107043.
- [25] Zhou, L., Zhao, R., and Yuan, W., “Application of improved $k\text{-}\omega\text{-}\gamma$ transition model to hypersonic complex configurations,” AIAA Journal, Vol. 57, No. 5, 2019, pp. 2214–2221.
- [26] Gosin, S. A., Coder, J. G., Galbraith, M. C., Allmaras, S. R., and Wyman, N. J., “Assessment of amplification factor transport transition modeling using output-based mesh adaptation,” AIAA Journal, 2025, pp. 1–24.
- [27] Krumbein, A. M., François, D. G., and Krimmelbein, N., “Transport-based transition prediction for the common research model natural laminar flow configuration,” Journal of Aircraft, Vol. 59, No. 6, 2022, pp. 1562–1573.
- [28] Liu, K., Wang, Y., Song, W.-P., and Han, Z.-H., “A two-equation local-correlation-based laminar-turbulent transition modeling scheme for external aerodynamics,” Aerospace Science and Technology, Vol. 106, 2020, p. 106128.
- [29] Choi, J. H., and Kwon, O. J., “Enhancement of a Correlation-Based Transition Turbulence Model for Simulating Crossflow Instability,” AIAA Journal, Vol. 53, No. 10, 2015, pp. 3063–3072. <https://doi.org/10.2514/1.J053887>.
- [30] Grabe, C., Shengyang, N., and Krumbein, A., “Transport modeling for the prediction of crossflow transition,” AIAA Journal, Vol. 56, No. 8, 2018, pp. 3167–3178.
- [31] Xu, J., Han, X., Qiao, L., Bai, J., and Zhang, Y., “Fully local amplification factor transport equation for stationary crossflow instabilities,” AIAA Journal, Vol. 57, No. 7, 2019, pp. 2682–2693.
- [32] Qin, Y., and Yu, X., “Predicting crossflow induced transition with laminar kinetic energy transition model,” International Journal of Heat and Fluid Flow, Vol. 81, 2020, p. 108522.
- [33] Kovalev, R., Kudryavtsev, V., and Churakov, D., “On modeling of laminar-turbulent transition in supersonic flows with engineering correlations and Reynolds-averaged Navier-Stokes equations,” Progress in Flight Physics–Volume 7, Vol. 7, 2015, pp. 525–548.

- [34] Shen, J., Wang, Y., Zhang, J., Xu, J., and Bai, J., “A novel local-variable-based transition-turbulence model for underwater boundary layers with temperature gradient effects,” Engineering Applications of Computational Fluid Mechanics, Vol. 19, No. 1, 2025, p. 2559109.
- [35] Menter, F. R., Smirnov, P. E., Liu, T., and Avancha, R., “A one-equation local correlation-based transition model,” Flow, Turbulence and Combustion, Vol. 95, No. 4, 2015, pp. 583–619.
- [36] Stewartson, K., “Further solutions of the Falkner-Skan equation,” Mathematical proceedings of the cambridge philosophical society, Vol. 50, Cambridge University Press, 1954, pp. 454–465.
- [37] Cooke, J., “The boundary layer of a class of infinite yawed cylinders,” Mathematical proceedings of the Cambridge philosophical society, Vol. 46, Cambridge University Press, 1950, pp. 645–648.
- [38] Liu, Z., “Compressible Falkner–Skan–Cooke boundary layer on a flat plate,” Physics of Fluids, Vol. 33, No. 12, 2021.
- [39] Mack, L. M., “Boundary-layer linear stability theory,” Technical report, Advisory Group for Aerospace Research and Development, Neuilly-sur-Seine, France, 1984. ADP004046-051.
- [40] Danabasoglu, G., and Biringen, S., “A Chebyshev Matrix Method for the Spatial Modes of the Orr–Sommerfeld Equation,” International Journal for Numerical Methods in Fluids, Vol. 11, No. 7, 1990, pp. 1033–1037. <https://doi.org/10.1002/flid.1650110709>.
- [41] Menter, F. R., “Two-equation eddy-viscosity turbulence models for engineering applications,” AIAA Journal, Vol. 32, No. 8, 1994, pp. 1598–1605. <https://doi.org/10.2514/3.12149>.
- [42] Menter, F. R., Kuntz, M., Langtry, R., et al., “Ten years of industrial experience with the SST turbulence model,” Turbulence, heat and mass transfer, Vol. 4, No. 1, 2003, pp. 625–632.
- [43] Schubauer, G. B., and Klebanoff, P. S., “Contributions on the mechanics of boundary-layer transition,” Technical Report NACA-TR-1289, NASA, 1956. <https://doi.org/10.4271/911003>.